

See discussions, stats, and author profiles for this publication at: <https://www.researchgate.net/publication/243374576>

Hierarchically Porous Gd 3+ -Doped CeO 2 Nanostructures for the Remarkable Enhancement of Optical and Magnetic Properties

ARTICLE *in* THE JOURNAL OF PHYSICAL CHEMISTRY C · JANUARY 2009

Impact Factor: 4.77 · DOI: 10.1021/jp804572t · Source: OAI

CITATIONS

55

READS

32

4 AUTHORS, INCLUDING:



Yexiang Tong

Sun Yat-Sen University

297 PUBLICATIONS 8,173 CITATIONS

SEE PROFILE



Open Archive Toulouse Archive Ouverte (OATAO)

OATAO is an open access repository that collects the work of Toulouse researchers and makes it freely available over the web where possible.

This is an author -deposited version published in: <http://oatao.univ-toulouse.fr/>
Eprints ID: 3836

To link to this article:

URL : <http://dx.doi.org/10.1021/jp804572t>

To cite this version: Li, Gao-Ren and Qu, Dun-Lin and Arurault, Laurent and Tong, Ye-Xiang (2009) *Hierarchically Porous Gd³⁺-Doped CeO₂ Nanostructures for the Remarkable Enhancement of Optical and Magnetic Properties*. The Journal of Physical Chemistry C, vol. 113 (n° 4). pp. 1235-1241. ISSN 1089-5639

Any correspondence concerning this service should be sent to the repository administrator:
staff-oatao@inp-toulouse.fr

Hierarchically Porous Gd³⁺-Doped CeO₂ Nanostructures for the Remarkable Enhancement of Optical and Magnetic Properties

Gao-Ren Li,^{*,†,‡} Dun-Lin Qu,[†] Laurent Arurault,[§] and Ye-Xiang Tong^{*,†}

MOE of Key Laboratory of Bioinorganic and Synthetic Chemistry, School of Chemistry and Chemical Engineering, Institute of Optoelectronic and Functional Composite Materials, Sun Yat-Sen University, Guangzhou 510275, China, State Key Laboratory of Rare Earth Materials Chemistry and Applications, Beijing 100871, China, and CIRIMAT-LCMIE, Université Paul Sabatier, 31062 Cedex 9, France

Rare earth ion-doped CeO₂ has attracted more and more attention because of its special electrical, optical, magnetic, or catalytic properties. In this paper, a facile electrochemical deposition route was reported for the direct growth of the porous Gd-doped CeO₂. The formation process of Gd-doped CeO₂ composites was investigated. The obtained deposits were characterized by SEM, EDS, XRD, and XPS. The porous Gd³⁺-doped CeO₂ (10 at% Gd) displays a typical type I adsorption isotherm and yields a large specific surface area of 135 m²/g. As Gd³⁺ ions were doped into CeO₂ lattice, the absorption spectrum of Gd³⁺-doped CeO₂ nanocrystals exhibited a red shift compared with porous CeO₂ nanocrystals and bulk CeO₂, and the luminescence of Gd³⁺-doped CeO₂ deposits was remarkably enhanced due to the presence of more oxygen vacancies. In addition, the strong magnetic properties of Gd-doped CeO₂ (10 at% Gd) were observed, which may be caused by Gd³⁺ ions or more oxygen defects in deposits. In addition, the catalytic activity of porous Gd-doped CeO₂ toward CO oxidation was studied.

1. Introduction

At present, the synthesis of ceria (CeO₂) nanostructures has aroused much interest because of a wide range of applications such as oxygen gas sensors, solid electrolytes in solid oxide fuel cells, phosphor/luminescence, catalysts for three-way automobile exhaust systems, and ultraviolet absorbers.¹ For some practical applications, the dopants, such as transition and non-transition metal ions, may be introduced into CeO₂ lattices for enhancing its optical properties or increasing its temperature stability and ability to store and release oxygen.² Recently attention has been focused on the preparation of rare earth ion-doped CeO₂ because of its special electrical, optical, magnetic or catalytic properties.³ For instance, the Eu³⁺(Sm³⁺, Tb³⁺)-doped CeO₂ nanocrystals showed remarkably enhanced photoluminescence (PL) intensity with respect to the CeO₂ nanocrystals due to the increased concentration of oxygen vacancies in the CeO₂ nanocrystals.⁴ Gd-doped CeO₂ has shown potential applications in the next generation of compact solid oxide fuel cells for their enhancement in oxygen-exchange processes and associated catalytic reactions.⁵

It is well-known that the performance of ceria-based materials is largely due to the ease in generating Ce³⁺ from Ce⁴⁺.⁶ In addition, the innate properties of ceria-based materials may be further amplified by producing ceria in nanostructured forms.⁷ Therefore, the synthesis of various nanostructures of ceria-based materials and their physical and chemical properties have been widely reported.⁸ In the past decade, there has been the tendency toward the development of novel, well-structured, and porous nanostructures, which have the ability to enhance the material properties by increasing the surface-area or providing channels.

For example, in the field of solid oxide fuel cells, a porous electrode structure is favorable for a rapid flux of gases through the pores, fast transport of ionic and electronic carriers through the solid phase, and efficient electrochemical reactions at the interfaces. However, at present there are relatively few reports on the preparation and characterization of porous rare earth ion-doped CeO₂ nanostructures.

Various methods, such as hydrothermal synthesis, spray pyrolysis, surfactant-templated synthesis, coprecipitation, and combustion synthesis, have been put forward for the synthesis of diverse CeO₂-based nanomaterials.⁹ However, the above methods often required relatively high reaction temperatures (100–1000 °C), special equipment, or multiple reaction steps. In addition, the prepared materials with high specific surface area are prone to agglomeration and exhibit broad pore size distributions, including, in some cases, small 1D pores.¹⁰ The process of sintering at high temperature will lead to the loss of surface area and oxygen storage capacity of CeO₂-based materials. Therefore, the preparation of CeO₂-based materials with high specific surface area by the sintering process is still not well-known technology.¹¹ Here we investigated an electrochemical deposition route for the preparation of hierarchically porous Gd-doped CeO₂ at room temperature, providing a facile and low-cost route for the synthesis of high-quality porous Gd-doped CeO₂ foam nanostructures in high yield. These as-prepared hierarchically porous Gd-doped CeO₂ nanostructures have shown a remarkable enhancement of optical and magnetic properties. In addition, we also have studied catalytic properties of Gd-doped CeO₂.

2. Experimental Section

The electrochemical deposition was carried out in a solution of 0.01 M Ce(NO₃)₃–0.01 M Gd(NO₃)₃–0.1 M NH₄NO₃. In this experiment a simple three-electrode cell was used in our

* Corresponding author. E-mail: ligaoren@mail.sysu.edu.cn and chedhx@mail.sysu.edu.cn.

[†] Sun Yat-Sen University.

[‡] State Key Laboratory of Rare Earth Materials Chemistry and Applications.

[§] Université Paul Sabatier.

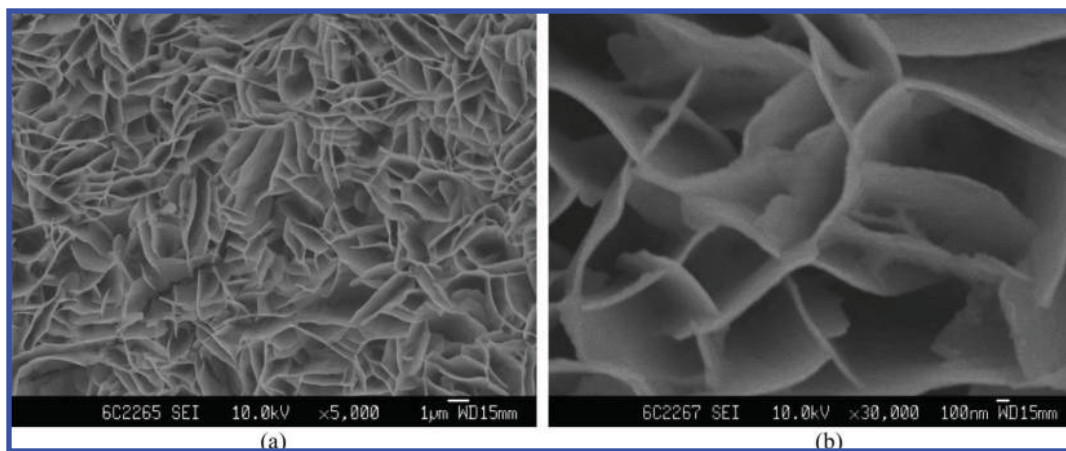


Figure 1. SEM images of porous CeO₂ prepared in a solution of 0.02 mol/L Ce(NO₃)₃ + 0.1 mol/L NH₄NO₃ with current density of 1.0 mA/cm² with different magnifications: (a) $\times 5\ 000$; (b) $\times 30\ 000$.

experiments. A highly pure Pt foil (99.99 wt %, 0.25 cm²) was used as the auxiliary electrode. A saturated calomel electrode (SCE) was used as the reference electrode that was connected to the cell with a double salt bridge system. All the electrochemical deposition experiments were carried out in a configured glass cell at room temperature, in which a Cu plate (99.99 wt %, 0.5 cm²) served as the substrate. Before electrodeposition, Cu substrate was cleaned ultrasonically in 0.1 M HCl, distilled water, and acetone and then rinsed in distilled water again. The structures of products were characterized by X-ray diffractometry (D/MAX 2200 VPC with Cu K α radiation). An Oxford Instrument's INCA energy-dispersive spectrometer (EDS) was employed to analyze chemical composition. Microstructures of the deposits were characterized by field emission scanning electron microscopy (FE-SEM; JSM-6330F). The X-ray photoelectron spectroscopy (XPS, ESCALAB 250) was used to assess the chemical state and surface composition of the deposits.

The UV–vis spectra of the samples were recorded on a UV–vis–NIR spectrophotometer (UV-3150). The photoluminescence (PL) spectra were carried out by spectrofluorophotometer (RF-5301PC) at room temperature. The magnetic property measurement system (MPMS XL-7) was used to investigate the magnetic behaviors of Ce_{0.9}Gd_{0.1}O_{2- δ} composites. The samples were also characterized by Brunauer, Emmett, and Teller (BET) nitrogen sorption surface area measurements (Micromeritics ASAP 2010). Specific surface areas of the prepared deposits were calculated by the Brunauer–Emmett–Teller (BET) method, and pore sizes were calculated by using the Barrett, Joyner, and Halenda (BJH) method (for large pores) or density functional theory (DFT) method (for small pores) on the basis of the adsorption branch of nitrogen sorption isotherms. Catalytic tests were carried out in a conventional fixed-bed quartz microreactor (8 mm in outer diameter) at atmospheric pressure. The system was first purged with high-purity N₂ gas (40 mL min⁻¹) and then a gas mixture of CO/O₂/N₂ (1:20:79) was introduced into the reactor, which contained 40-mg samples at a flow rate of 40 mL min⁻¹. Gas samples were analyzed by an online gas chromatography, using a Porapak Q column for the separation of CO₂ and CO and a 5A Molecular Sieve column for the separation of N₂ and O₂. The catalytic performance was evaluated at various temperatures.

3. Results and Discussion

Figure 1 shows the SEM images of the CeO₂ deposits prepared in a solution of 0.02 M Ce(NO₃)₃–0.1 M NH₄NO₃

with current density of 1.0 mA/cm². The porous CeO₂ foam structures were successfully prepared. The thickness of walls is about 50 nm as shown in Figure 1b. The sizes of pores are between 3 and 8 μ m. The porous structures of the deposits can be manipulated by adding Gd(NO₃)₃ into deposition solution. When the electrodeposition was carried out in a solution of 0.01 M Ce(NO₃)₃–0.01 M Gd(NO₃)₃–0.10 M NH₄NO₃ with a current density of 1.0 mA/cm², the porous Gd-doped CeO₂ foam structures were prepared, and the SEM images were shown in Figure 2. It can be easily found that the foam structures have a higher density of pores, and the sizes of pores are smaller, which are about 200–500 nm.

EDS measurement was carried out at a number of locations throughout the specimens, and a representative EDS pattern of porous Gd-doped CeO₂ foam structure was shown in Figure 3. An oxygen peak at about 0.5 keV and Ce signals at about 0.9, 4.9, and 6.0 keV were observed, respectively. The Gd peaks at 0.9, 6.0, and 8.1 keV were observed. The EDS results therefore demonstrated that O, Ce, and Gd were electrodeposited. The composition analysis showed an approximate atom ratio of Ce to Gd was about 9:1 in the Gd-doped CeO₂ composites. For the element Ce, there are two different oxidation states Ce³⁺ and Ce⁴⁺. The Ce⁴⁺ oxidation state is more stable than Ce³⁺ in the presence of air. It is well-known that there coexists a small amount of Ce³⁺ at the surface of CeO₂.¹² The results of XPS analyses of Gd-doped CeO₂ deposits (10 atom % Gd) were shown in Figure 4. The presence of Ce³⁺ ions in the CeO₂ nanocrystals has been confirmed by XPS analysis, with Ce³⁺ peaks found at 883 and 901 eV in Figure 4a(1). The binding energies of Ce³⁺ ions in Gd-doped CeO₂ deposits are red-shifted compared to bulk CeO₂.¹³ The XPS peaks centered at 1188 and 1219 eV in Figure 4b can be attributed to the Gd³⁺ contribution. In addition, the XPS peak centered at 529.3 eV in Figure 4c can be attributed to the O²⁻ contribution.¹⁴ Therefore, the XPS results demonstrated the obtained deposits were Gd³⁺-doped CeO₂ with a small quantity of Ce³⁺ oxidation state. The XPS spectrum of porous Gd-doped CeO₂ deposits (12 atom % Gd) was shown in Figure 4a(2). Although the peaks of Ce⁴⁺ in Figure 4a(2) are almost the same as those in Figure 4a(1), the peaks of Ce³⁺ in Figure 4a(2) are obviously lower than those in Figure 4a(1), indicating the variation of Ce(III)/Ce(IV) ratios.

The formation process of Gd-doped CeO₂ composites (10 atom % Gd) was investigated as follows. During the electrodeposition, OH⁻ ions were formed via the electroreduction of NO₃⁻ ions in deposition solution on the surface of the cathode. These produced OH⁻ ions will result in the formation

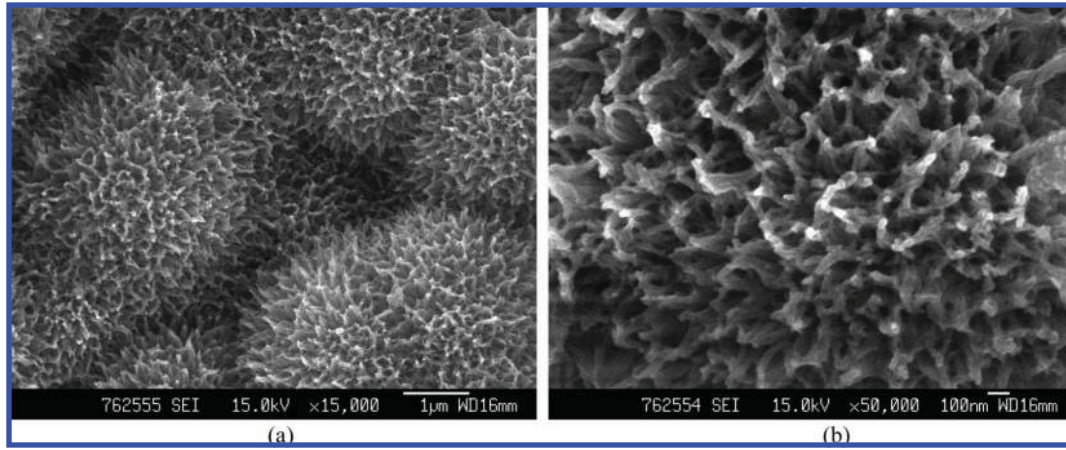


Figure 2. SEM images of porous Gd-doped CeO₂ prepared in a solution of 0.01 M Ce(NO₃)₃–0.01 M Gd(NO₃)₃–0.1 M NH₄NO₃ with current density of 1.0 mA/cm²: (a) ×15 000; (b) ×50 000.

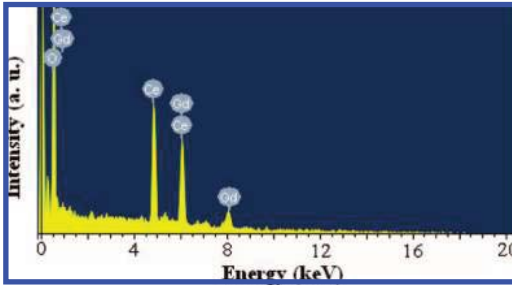
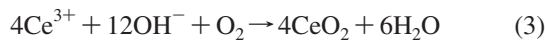
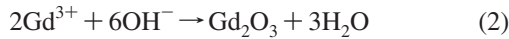


Figure 3. EDS pattern of the porous Gd-doped CeO₂ composite foam structures.

of CeO₂ and Gd₂O₃, and the formation processes of CeO₂ and Gd₂O₃ can be expressed as eqs 1, 2, and 3. It is well-known that the electrochemical deposition allows mixing of the chemicals at the atomic level. Therefore, when the electrodeposition was carried out, the mixed CeO₂ and Gd₂O₃ at the atomic level were always obtained, and accordingly the homogeneous Gd-doped CeO₂ composites were prepared (eq 4).



Further characterization by X-ray powder diffraction was carried out, and the XRD patterns of CeO₂ (a) and Gd³⁺-doped CeO₂ (10 atom % Gd) (b) porous structures were shown in Figure 5. The results of XRD indicate that the CeO₂ nanocrystals are well-crystallized. The peaks corresponding to the CeO₂ (111), (200), (220), and (311) planes were observed, and all these diffraction peaks of CeO₂ can be indexed as a face-centered cubic-phase as identified by using the standard data JCPDS 34-0394. Here, we should notice that the XRD peaks of CeO₂ in the 2θ range from 25° to 70° exhibit the broadened peaks with a little shift toward smaller angles. According to the Scherrer equation (i.e., $D = K\lambda/(\beta \cos\theta)$ (where λ is the wavelength of the X-ray radiation, K is a constant taken as 0.89, θ is the diffraction angle, and β is the full width at half-maximum), the strongest peak (111) at $2\theta = 28.8^\circ$ and the peak (220) at $2\theta = 47.4^\circ$ were used to calculate the average crystallite size of CeO₂ nanocrystals, determined to be around 5.0 nm. The cell parameter (a) is calculated as about 0.5441 nm, a little larger than that of bulk CeO₂ (0.5411 nm). The larger cell

parameter may be attributed to the lattice expansion effect resulting from the increased Ce³⁺ ions and oxygen vacancies.¹⁵ For Gd³⁺-doped CeO₂ porous structures, the XRD pattern in Figure 5b was almost the same as that of CeO₂ porous structures, and all diffraction peaks can be indexed to the face-centered cubic-phase of CeO₂. The average crystal size of Gd³⁺-doped CeO₂ nanocrystals was estimated as about 4.5 nm by the Scherrer equation. However, the diffraction peaks of Gd or Gd₂O₃ were not observed in the XRD pattern, indicating Gd³⁺ ions entering into CeO₂ lattices. The cell parameter values were calculated as about 0.5429 nm, which is a little smaller than that of porous CeO₂. This may be due to the lattice constriction effect resulting from Gd³⁺ ions. This can be attributed to the replacement of Ce³⁺ by trivalent Gd³⁺ ions. As we all know, the ionic radius of Gd³⁺ (107.8 pm) is smaller than those of Ce³⁺ (115 pm). Therefore, the lattice constricts upon Gd³⁺ doping will happen.

The porous CeO₂ and Gd³⁺-doped CeO₂ (10 atom % Gd) have been studied by the Raman scattering method as shown in Figure 6. For the porous CeO₂, one high and sharp peak at 461 cm^{−1} is clearly observed in Figure 6a, which can be assigned to *F*2g symmetry because of a symmetric breathing mode of the oxygen atoms around the cerium ions.^{16,17} The Raman shift is about 3 cm^{−1} compared with the bulk CeO₂ (464 cm^{−1}). It is well-known that the change of the Raman peak's position can be attributed to the changes of bond length or lattice spacing. For porous CeO₂, the shift of the Raman peak is related to the enlarged lattice space because of the smaller size of CeO₂ crystals (5.0 nm).^{18–20} In addition, the Raman shift also can be calculated by the following equation:¹⁶

$$\Delta\omega = -3\gamma\omega_0\Delta a/a_0 \quad (5)$$

where γ is the Grüneisen constant, ω_0 is the Raman frequency of bulk CeO₂, Δa is the change in lattice constant, and a_0 is the lattice constant of bulk CeO₂ (0.5411 nm). The Raman frequency shift $\Delta\omega$ can be calculated as about −3.32 cm^{−1}, which is very close to the above experimental value. However, for the porous Gd³⁺-doped CeO₂, the first-order peak was shifted to 456 cm^{−1}, and this peak became broad compared with that of porous CeO₂. For porous Gd³⁺-doped CeO₂, the shift of the Raman peak is also related to the change in lattice spacing caused by the constriction of the lattice upon Gd-doping and to the change in the atomic geometry arising from Gd-doping. These lead to a larger shift compared with the porous CeO₂. In addition, one weak peak at about 602 cm^{−1} was observed, which could be associated with the presence of the Gd element.

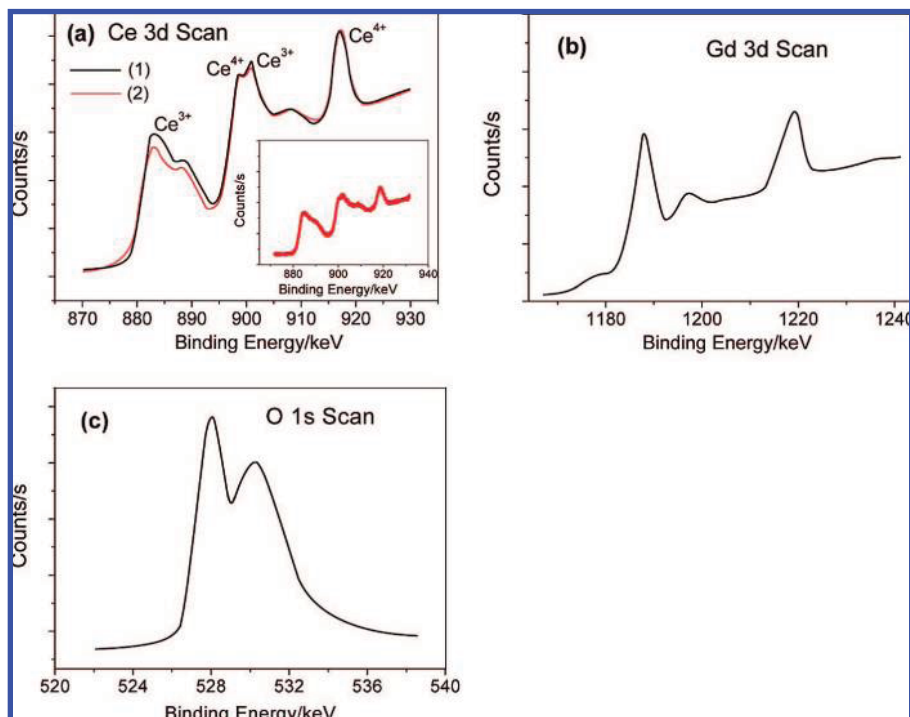


Figure 4. XPS spectra of Gd-doped CeO₂: (a) Ce 3d in Ce_{0.9}Gd_{0.1}O_{2-δ} (1); Ce 3d in Ce_{0.88}Gd_{0.12}O_{2-δ} (2); Ce 3d of porous CeO₂ (inset); (b) Gd 3d; and (c) O1s spectra in Ce_{0.9}Gd_{0.1}O_{2-δ}.

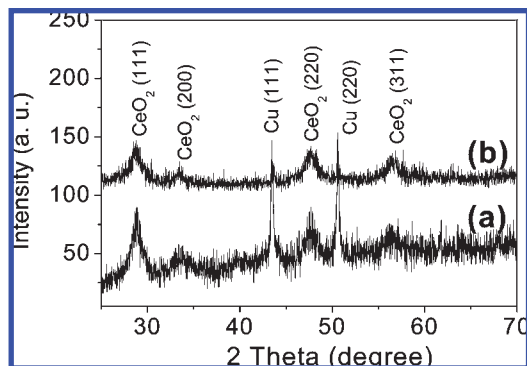


Figure 5. XRD patterns of (a) Gd-doped CeO₂ (10 atom % Gd) and (b) CeO₂ porous structures.

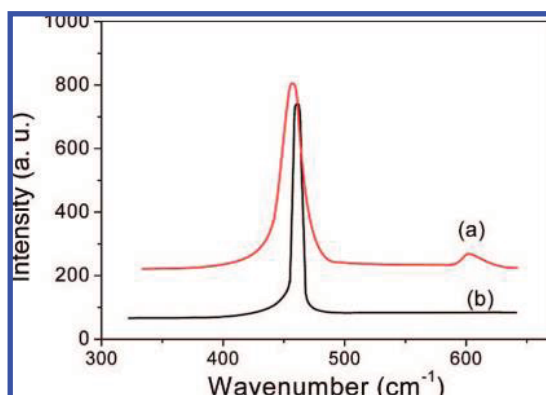


Figure 6. Raman spectra of (a) Gd-doped CeO₂ (10 atom % Gd) and (b) CeO₂ porous structures taken at room temperature.

The porosity of the synthesized porous CeO₂ and Gd³⁺-doped CeO₂ (10 atom % Gd) were characterized by nitrogen sorption analysis, using standard Brunauer–Emmett–Teller (BET) techniques. The nitrogen adsorption and desorption isotherms and the resulting pore size distributions of porous CeO₂ and Gd³⁺-

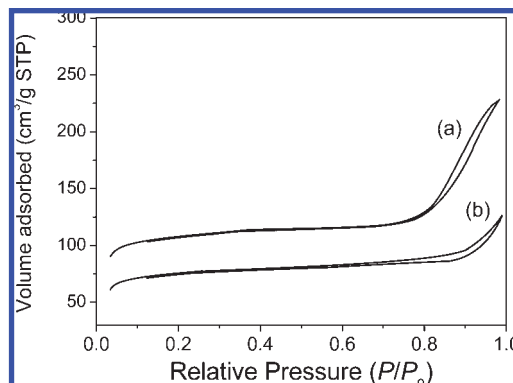


Figure 7. N₂ adsorption–desorption isotherms of (a) Gd-doped CeO₂ (10 atom % Gd) and (b) CeO₂ porous structures.

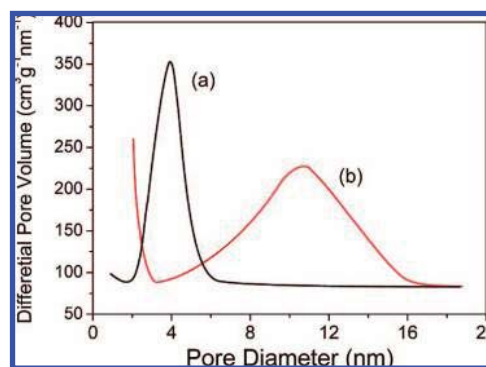


Figure 8. DFT pore size distributions of (a) Gd-doped CeO₂ (10 atom % Gd) and (b) CeO₂ porous structures.

doped CeO₂ are shown in Figures 7 and 8, respectively. The porous CeO₂ and Gd³⁺-doped CeO₂ both display a typical type I adsorption isotherm and yield specific surface areas of 93 and 135 m²/g, respectively. Thus, the specific surface area of porous Gd³⁺-doped CeO₂ was larger than that of porous CeO₂. The pore diameters of porous Gd³⁺-doped CeO₂ and CeO₂ are

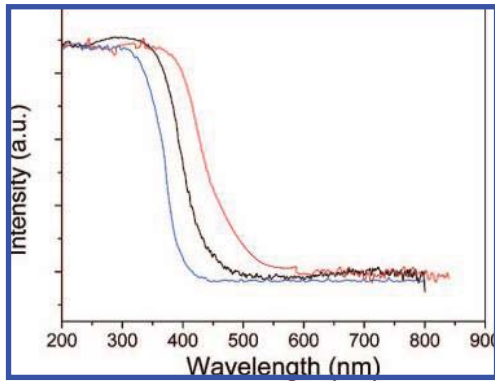


Figure 9. UV-vis absorption spectra of porous Gd-doped CeO₂ (10 atom % Gd) (red line), porous CeO₂ (blue line), and bulk CeO₂ (black line).

distributed with peaks centered at around 4 and 11 nm, respectively.

For the porous CeO₂, there is a strong absorption band below 400 nm in the spectrum as shown in Figure 9, which is due to the charge-transfer transition from O²⁻ (2p) to Ce⁴⁺ (4f) orbitals in CeO₂.²¹ However, the absorption spectrum of Gd³⁺-doped CeO₂ (10 atom % Gd) nanocrystals exhibits a red shift compared with porous CeO₂ nanocrystals and bulk CeO₂. For CeO₂ nanocrystals, it is well-known that there coexists a small amount of Ce³⁺ at the surface of CeO₂ and the fraction of Ce³⁺ ions increases with decreasing particle size.^{22,23} The presence of Ce³⁺ ions in the CeO₂ nanocrystals can be confirmed by XPS analysis as shown in Figure 4a. The valence change from Ce⁴⁺ to Ce³⁺ on the surface of nanocrystals might have some additional contributions to the absorption of CeO₂ nanocrystals because the change from +4 to +3 increases the charge-transfer gap between O 2p and Ce 4f bands, which leads to the blue-shift of absorption spectrum of CeO₂ nanocrystals compared with bulk CeO₂.²⁴ In addition, the average size of the obtained Gd³⁺-doped CeO₂ nanocrystals is about 5.0 nm, which is smaller than the estimated exciton Bohr radius for CeO₂ (7–8 nm).²⁵ Therefore, a quantum confinement effect possibly takes place, which contributes to the blue-shift of the absorption edge of the porous CeO₂. When Gd³⁺ was doped into CeO₂, the peaks of Ce⁴⁺ 3d_{3/2} and Ce⁴⁺ 3d_{5/2} become stronger than that of the undoped CeO₂ nanocrystals as shown in the XPS spectrum in the inset in Figure 4a, while those of Ce³⁺ 3d_{3/2} and Ce³⁺ 3d_{5/2} are relatively weak, indicating the decrease of the Ce³⁺ fraction on the surface of CeO₂. This may be attributed to the replacement of Ce³⁺ by trivalent Gd³⁺ ions. Accordingly, the contribution of blue-shifting arising from the Ce⁴⁺ to Ce³⁺ valence change will become small. Therefore, the red-shifting occurs in the absorption spectrum of Gd³⁺-doped CeO₂ (10 atom % Gd) nanocrystals compared with that of CeO₂ nanocrystals. According to eq 6, the optical band gaps (E_g) of porous CeO₂ and Gd³⁺-doped CeO₂ can be estimated by using the data for the absorption spectra:

$$ahv = C(hv - E_g)^n \quad (6)$$

Here $h\nu$ is photon energy, α is the absorption coefficient, C is the constant, $n = 2$ for an indirectly allowed transition, and $n = 1/2$ for a directly allowed transition.²⁶ The direct band gap values of porous CeO₂ and Gd³⁺-doped CeO₂ nanocrystals can be determined as about 3.10 and 2.48 eV, respectively.

The photoluminescent (PL) properties of porous CeO₂ and Gd³⁺-doped CeO₂ (10 atom % Gd) were also investigated. Figure 10 shows the excitation (a) and emission (b) spectra of

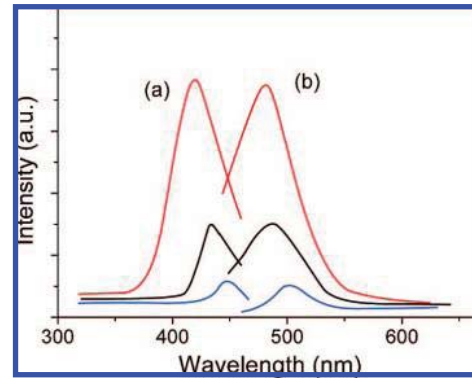


Figure 10. Excitation (a) and emission (b) spectra of porous Gd-doped CeO₂ (10 atom % Gd) (red line), porous CeO₂ (black line), and bulk CeO₂ (blue line) in hexane solution.

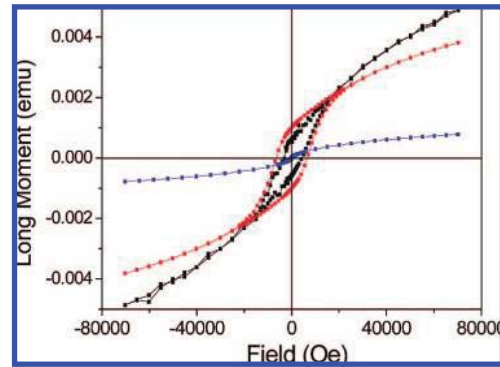


Figure 11. The magnetization hysteresis loops of porous Gd-doped CeO₂ (10 atom % Gd) (red line), porous CeO₂ (black line), and bulk CeO₂ (blue line) at 5 K.

porous Gd³⁺-doped CeO₂ (red lines) and CeO₂ (black lines). The band emission of CeO₂ can be remarkably enhanced by doping Gd³⁺ into CeO₂ lattices. According to the above results, the emissions of CeO₂ and Gd³⁺ were not detected in the Gd³⁺-doped CeO₂, and the luminescence spectra shown in Figure 10 are from oxygen vacancies.⁴ The extrinsic oxygen vacancies are generated in the fluorite lattice of CeO₂ nanocrystals because of the existence of Ce³⁺.⁴ When Gd³⁺ ions are doped into CeO₂ nanocrystals, the fraction of trivalent Ce³⁺ ions will be decreased because of the replacement of Ce³⁺ by Gd³⁺ ions; however, the oxygen vacancy concentration in CeO₂:Gd³⁺ nanocrystals must be much higher because the doping concentration of Gd³⁺ is much larger than the fraction of Ce³⁺ in undoped nanocrystals.⁴ Therefore, when Gd³⁺ ions were doped into CeO₂ lattice, the enhancement of luminescence of Gd³⁺-doped CeO₂ deposits is attributed to the increase of oxygen vacancies.

Figure 11 shows the magnetization hysteresis loops of porous CeO₂ and Gd³⁺-doped CeO₂ (10 atom % Gd) at 5 K. As we all know, the stoichiometric CeO₂ should be nonmagnetic. However, the obvious magnetic property was observed for the prepared porous CeO₂ and Gd-doped CeO₂. The coercivity field (H_c) and the remanent magnetization (M_r) of Gd-doped CeO₂ were larger than those of porous CeO₂. For porous Gd³⁺-doped CeO₂, the H_c is about 6838 Oe, and M_r is about 1.02×10^{-3} emu at 5 K. What leads to the stronger magnetic property of the porous Gd³⁺-doped CeO₂? The mechanism of the origin of magnetism in doped CeO₂ is still under investigation. It has been proved that the oxygen defects and Ce³⁺ ions existed in porous CeO₂ deposits by XRD and XPS, and the Ce³⁺ ions in deposits can lead to the magnetic properties of CeO₂.^{13b,27}

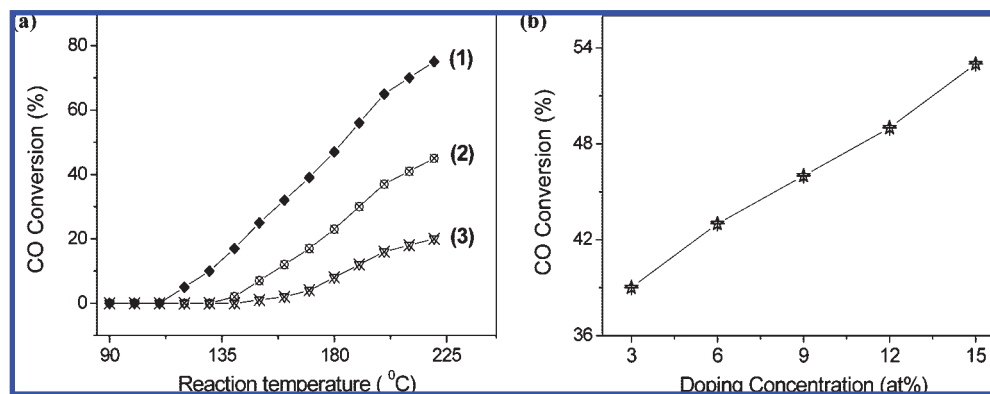


Figure 12. (a) CO conversion as a function of temperature for the as-deposited porous Gd-doped CeO₂ (10 atom % Gd) (1), porous CeO₂ (2), and CeO₂ nanoparticles (3). (b) CO conversion as a function of doping concentration for the as-deposited porous Gd-doped CeO₂ at 180 °C.

Therefore, the stronger magnetic properties of Gd-doped CeO₂ may be caused by the higher concentration of Gd³⁺ ions in deposits.

CeO₂ is an important three-way catalyst, and we studied the catalytic activity of porous Gd-doped CeO₂ (10 at% Gd), porous CeO₂, and CeO₂ nanoparticles. Catalytic activities of CeO₂ samples as a function of reaction temperature are shown in Figure 12a. The CO conversion increases with increasing reaction temperature for all samples. It can be clearly observed that porous Gd-doped CeO₂ shows much higher activity than porous CeO₂ and CeO₂ nanoparticles. For porous Gd-doped CeO₂, a 47% CO conversion is achieved at 180 °C, while only 23% and 8% CO conversions are obtained at the same temperature for porous CeO₂ and CeO₂ nanoparticles, respectively. For the same CO conversion (20%), the reaction temperature for porous Gd-doped CeO₂ can be 30 and 76 °C lower than those for porous CeO₂ and CeO₂ nanoparticles, respectively. The large difference in catalytic activity can be partly due to the variation in surface area. It is well-known that the catalytic process is mainly related to the adsorption and desorption of gas molecules on the surface of catalyst.²⁸ Therefore, the porous structures with high surface area enable better contact with gas molecules, and accordingly show better catalytic performance compared with CeO₂ nanoparticles. In addition to the surface area, the oxygen vacancies in CeO₂ are also an important factor for better performance as they can act as promoting sites for CO conversion.^{1d} On the basis of the above results, the oxygen vacancy concentration in porous Gd-doped CeO₂ is much larger than those of porous CeO₂ and CeO₂ nanoparticles, which further promotes the catalytic performance of porous Gd-doped CeO₂. Figure 12b shows CO conversion as a function of doping concentration for the as-deposited porous Gd-doped CeO₂ at 180 °C, indicating oxidation ability increases with doping concentration.

4. Conclusions

In summary, a facile electrochemical deposition route was developed for the direct growth of porous Gd-doped CeO₂. The porous Gd³⁺-doped CeO₂ (10 atom % Gd) displays a typical type I adsorption isotherm and yields a specific surface area of 135 m²/g. The pore diameters of porous Gd³⁺-doped CeO₂ (10 atom % Gd) are distributed with peaks centered at around 4 nm. The XPS results demonstrated the obtained Gd³⁺-doped CeO₂ deposits have a small quantity of Ce³⁺ oxidation state. The optical band gap values of porous Gd³⁺-doped CeO₂ (10 atom % Gd) nanocrystals can be determined as 2.48 eV, which is much smaller than 3.10 eV of porous CeO₂. In addition, when

Gd³⁺ ions were doped into CeO₂ lattice, the luminescence of Gd³⁺-doped CeO₂ deposits was remarkably enhanced, which can be attributed to the rapid oxygen vacancy increase. The magnetic properties of porous CeO₂ may be caused by the Ce³⁺ ions in deposits, and the stronger magnetic properties of Gd-doped CeO₂ were caused by more RE³⁺ ions in deposits. Furthermore, better catalytic actives of porous Gd³⁺-doped CeO₂ nanocrystals were obtained compared with those of porous CeO₂ and CeO₂ nanoparticles.

Acknowledgment. This work was supported by the Natural Science Foundation of China (Grant No. 20603048 and 20873184), the Guangdong Province Science & Technology Development Program (2008B010600040), and the Foundation of Potentially Important Natural Science Research of Sun Yat-Sen University.

References and Notes

- (1) (a) Nolan, M.; Watson, G. W. *J. Phys. Chem. B* **2006**, *110*, 2256. (b) Nolan, M.; Watson, G. W. *J. Phys. Chem. B* **2006**, *110*, 16600. (c) Feng, X.; Sayle, D. C.; Wang, Z. L.; Paras, M. S.; Santora, B.; Sutorik, A. C.; Sayle, T. X. T.; Yang, Y.; Ding, Y.; Wang, X. D.; Her, Y. S. *Science* **2006**, *312*, 1504–1508. (d) Ho, C.; Yu, J. C.; Kwong, T.; Mak, A. C.; Lai, S. *Chem. Mater.* **2005**, *17*, 4514–4522. (e) Tarnuzzer, R. W.; Colon, J.; Patil, S.; Seal, S. *Nano Lett.* **2005**, *5*, 2573. (f) Leah, R. T.; Brandon, N. P.; Aguiar, P. J. *Power Sources* **2005**, *145*, 336. (g) Morshed, A. H.; Moussa, M. E.; Bedair, S. M.; Leonard, R.; Liu, S. X.; El-Masry, N. *Appl. Phys. Lett.* **1997**, *70*, 1647. (h) Laha, S. C.; Ryoo, R. *Chem. Commun.* **2003**, 2138.
- (2) (a) Matolin, V.; Sedlacek, L.; Matolinova, I.; Sutara, F.; Skala, T.; Smid, B.; Libra, J.; Nehasil, V.; Prince, K. C. *J. Phys. Chem. C* **2008**, *112*, 3751–3758. (b) Romero-Sarria, F.; Martinez, T.; L. M.; Centeno, M. A.; Odriozola, J. A. *J. Phys. Chem. C* **2007**, *111*, 14469–14475. (c) Reddy, B. M.; Bharali, P.; Saikia, P.; Khan, A.; Loridant, S.; Muhler, M.; Grunert, W. *J. Phys. Chem. C* **2007**, *111*, 1878–1881. (d) Perkas, N.; Rotter, H.; Vradman, L.; Landau, M. V.; Gedanken, A. *Langmuir* **2006**, *22*, 7072–7077. (e) Li, G.; Mao, Y.; Li, L.; Feng, S.; Wang, M.; Yao, X. *Chem. Mater.* **1999**, *11*, 1259–1266. (f) Abimanyu, H.; Ahn, B. S.; Kim, C. S.; Yoo, K. S. *Ind. Eng. Chem. Res.* **2007**, *46*, 7936–7941. (g) de Carolis, S.; Pascual, J. L.; Pettersson, L. G. M.; Baudin, M.; Wojcik, M.; Hermansson, K.; Palmqvist, A. E. C.; Muhammed, M. *J. Phys. Chem. B* **1999**, *103*, 7627–7636.
- (3) (a) Linares, R. C. *J. Opt. Soc. Am.* **1966**, *56*, 1700. (b) Yugami, H.; Nakajima, A.; Ishigame, M.; Suemoto, T. *Phys. Rev. B* **1991**, *44*, 4862. (c) Fujihara, S.; Oikawa, M. *J. Appl. Phys.* **2004**, *95*, 8002. (d) Maher, R. C.; Cohen, L. F.; Lohsoontorn, P.; Brett, D. J. L.; Brandon, N. P. *J. Phys. Chem. A* **2008**, *112*, 1497–1501. (e) Suzuki, T.; Kosacki, I.; Petrovsky, V.; Anderson, H. U. *J. Appl. Phys.* **2002**, *91*, 2308–2313. (f) Rupp, J. L. M.; Drobek, T.; Rossi, A.; Gauckler, L. J. *Chem. Mater.* **2007**, *19*, 1134–1142.
- (4) Wang, Z.; Quan, Z.; Lin, J. *Inorg. Chem.* **2007**, *46*, 5237–5242.
- (5) (a) Sahibzada, M.; Steele, B. C. H.; Zheng, K.; Rudkin, R. A.; Metcalfe, I. S. *Catal. Today* **1997**, *38*, 459. (b) Perez-Coll, D.; Nunez, P.; Ruiz-Morales, J. C.; Pena-Martinez, J.; Frade, J. R. *Electrochim. Acta* **2007**, *52*, 2001. (c) Popovic, Z. V.; Dohcevic-Mitrovic, Z.; Konstantinovic, M. J.; Scepanovic, M. *J. Raman Spectrosc.* **2007**, *38*, 750.
- (6) Tschöpe, A. *J. Electroceram.* **2005**, *14*, 5–23.

- (7) Laberty-Robert, C.; Long, J. W.; Lucas, E. M.; Pettigrew, K. A.; Stroud, R. M.; Doescher, M. S.; Rolison, D. R. *Chem. Mater.* **2006**, *18*, 50–58.
- (8) (a) Ahniyaz, A.; Sakamoto, Y.; Bergström, L. *Cryst. Growth Des.* **2008**, *8*, 1798–1800. (b) Du, N.; Zhang, H.; Chen, B.; Ma, X.; Yang, D. *J. Phys. Chem. C* **2007**, *111*, 12677–12680. (c) Liang, X.; Wang, X.; Zhuang, Y.; Xu, B.; Kuang, S.; Li, Y. *J. Am. Chem. Soc.* **2008**, *130*, 2736–2737. (d) Natile, M. M.; Glisenti, A. *Chem. Mater.* **2005**, *17*, 3403–3414. (e) Ahniyaz, A.; Sakamoto, Y.; Bergström, L. *Cryst. Growth Des.* **2008**, *8*, 1798–1800. (f) Du, N.; Zhang, H.; Chen, B.; Ma, X.; Yang, D. *J. Phys. Chem. C* **2007**, *111*, 12677–12680. (g) Liang, X.; Wang, X.; Zhuang, Y.; Xu, B.; Kuang, S.; Li, Y. *J. Am. Chem. Soc.* **2008**, *130*, 2736–2737. (h) Natile, M. M.; Glisenti, A. *Chem. Mater.* **2005**, *17*, 3403–3414.
- (9) (a) Hirano, M.; Kato, E. *J. Am. Ceram. Soc.* **1996**, *79*, 777–780. (b) Gesser, H. D.; Goswami, P. C. *Chem. Rev.* **1989**, *89*, 765–788. (c) Masui, T.; Fujiwara, K.; Machida, K.; Adachi, G.; Sakata, T.; Mori, H. *Chem. Mater.* **1997**, *9*, 2197–2204. (d) Pijolat, M.; Viricelle, J. P.; Sosutelle, M. *Stud. Surf. Sci. Catal.* **1997**, *91*, 885–891. (e) Purohit, R. D.; Sharma, D.; Pillai, K. T.; Tyagi, A. K. *Mater. Res. Bull.* **2001**, *36*, 2711–2716.
- (10) Laberty-Robert, C.; Long, J. W.; Pettigrew, K. A.; Stroud, R. M.; Rolison, D. R. *Adv. Mater.* **2007**, *19*, 1734–1739.
- (11) Yuzhakova, T.; Rakić, V.; Guimon, C.; Auroux, A. *Chem. Mater.* **2007**, *19*, 2970–2981.
- (12) Tsunekawa, S.; Fukuda, T.; Kasuya, A. *Surf. Sci.* **2000**, *457*, L437.
- (13) (a) Bumajdad, A.; Zaki, M. I.; Eastoe, J.; Pasupulety, L. *Langmuir* **2004**, *20*, 11223–11233. (b) Li, G.-R.; Qu, D.-L.; Yu, X.-L.; Tong, Y.-X. *Langmuir* **2008**, *24*, 4254–4259.
- (14) (a) Salvi, A. M.; Decker, F.; Varsano, F.; Speranza, G. *Surf. Interface Anal.* **2001**, *31*, 255. (b) Huang, P. X.; Wu, F.; Zhu, B. L.; Gao, X. P.; Zhu, H. Y.; Yan, T. Y.; Huang, W. P.; Wu, S. H.; Song, D. Y. *J. Phys. Chem. B* **2005**, *109*, 19169–19174.
- (15) (a) Tsunekawa, S.; Sahara, R.; Kawazoe, Y.; Ishikawa, K. *Appl. Surf. Sci.* **1999**, *152*, 53. (b) Tsunekawa, S.; Ishikawa, K.; Li, Z. Q.; Kawazoe, Y.; Kasuya, A. *Phys. Rev. Lett.* **2000**, *85*, 3440. (c) Zhou, X.-D.; Huebner, W. *Appl. Phys. Lett.* **2001**, *79*, 3512. (d) Wu, L. J.; Wiesmann, H. J.; Moodenbaugh, A. R.; Klie, R. F.; Zhu, Y.; Welch, D. O.; Suenaga, M. *Phys. Rev. B* **2004**, *69*, 125415.
- (16) McBride, J. R.; Hass, K. C.; Poindexter, B. D.; Weber, W. H. *J. Appl. Phys.* **1994**, *76*, 2435.
- (17) Li, X. M.; Li, L. P.; Li, G. S.; Su, W. H. *Mater. Chem. Phys.* **2001**, *69*, 236.
- (18) Spanier, J. E.; Robinson, R. D.; Zhang, F.; Chan, S. W.; Herman, I. P. *Phys. Rev. B* **2001**, *64*, 245407.
- (19) Weber, W. H.; Hass, K. C.; McBride, J. R. *Phys. Rev. B* **1993**, *48*, 178.
- (20) Graham, G. W.; Weber, W. H.; Peters, C. R.; Usmen, R. *J. Catal.* **1991**, *130*, 310.
- (21) Zhang, Y. W.; Si, R.; Liao, C. S.; Yan, C. H.; Xiao, C. X.; Kou, Y. *J. Phys. Chem. B* **2003**, *107*, 10159.
- (22) Wu, L. J.; Wiesmann, H. J.; Moodenbaugh, A. R.; Klie, R. F.; Zhu, Y.; Welch, D. O.; Suenaga, M. *Phys. Rev. B* **2004**, *69*, 125415.
- (23) Tsunekawa, S.; Fukuda, T.; Kasuya, A. *Surf. Sci.* **2000**, *457*, L437.
- (24) Tsunekawa, S.; Fukuda, T.; Kasuya, A. *J. Appl. Phys.* **2000**, *87*, 1318.
- (25) Tsunekawa, S.; Wang, J.-T.; Kawazoe, Y. *J. Alloys Compd.* **2006**, *408–412*, 1145.
- (26) Yin, L.; Wang, X. Y. Q.; Pang, G. S.; Koltypin, Y.; Gedanken, A. *J. Colloid Interface Sci.* **2002**, *246*, 78.
- (27) Li, G.-R.; Qu, D.-L.; Tong, Y.-X. *Electrochem. Commun.* **2008**, *10*, 80–84.
- (28) Chen, G.; Xu, C.; Song, X.; Zhao, W.; Ding, Y.; Sun, S. *Inorg. Chem.* **2008**, *47*, 723–728.

JP804572T